Achieving work hardening by forming boundaries on the nanoscale in a Ti-based metallic glass matrix composite

J. Fan[1,2], W. Rao[3], J.W. Qiao[1, 2,*], P.K. Liaw[4], D. Şopu[5,6], D. Kiener[7], J. Eckert[6,7], G.Z. Kang[3], and Y.C. Wu[1,**]

[1]College of Materials Science and Engineering, Taiyuan University of Technology, Taiyuan 030024, China
[2]Key Laboratory of Interface Science and Engineering in Advanced Materials, Ministry of Education,
Taiyuan University of Technology, Taiyuan 030024, China
[3]Key Laboratory of Advanced Technologies of Materials, School of Mechanics and Engineering, Southwest
Jiaotong University, Ministry of Education of China,
Chengdu, Sichuan, 610031, China.
[4]Department of Materials Science and Engineering, The University of Tennessee, Knoxville, TN 37996-2200, USA
[5]Technische Universität Darmstadt, Institut für Materialwissenschaft, Fachgebiet
Materialmodellierung, Otto-Berndt-Strasse 3, D-64287 Darmstadt, Germany
[6]Erich Schmid Institute of Materials Science, Austrian Academy of Sciences, Jahnstraße 12, A-8700
Leoben, Austria
[7]Department Materials Physics, Montanuniversität Leoben, Jahnstraße 12, A-8700 Leoben, Austria

Abstract

Challenges of achieving work hardening in metallic glass matrix composites (MGMCs) always exist. In this study, we investigated the formation of boundaries (Please define what kinds of boundaries) on the nanoscale, which favors the work-hardening deformation in an *in-situ* $Ti_{41}Zr_{32}Ni_6Ta_7Be_{14}$ MGMC with β-Ti dendrites in a glassy matrix at room temperature. Microstructures of samples after tension were observed by high-resolution transmission electron microscopy (HRTEM) and X-ray diffraction (XRD). The work-hardening mechanism of the present composites involves: (1) the appearance of dense dislocation walls (DDWs), (2) the proliferation of shear bands, (3) the formation of boundaries at nanoscale, and (4) the interactions between hard and soft phases. A theoretical model combined with experimental data reveals the deformation mechanisms in the present work, proving that the *in-situ* dendrites with the outstanding hardening ability in the glass matrix can provide the homogeneous deformation under tensile loading at room temperature.

Keywords: Metallic glass matrix composites; Plastic deformation; Work hardening; Dense dislocation walls; Nanoscale boundaries

---

* Corresponding author. E-mail: qiaojunwei@gmail.com; ** Corresponding author. E-mail: wyc@tyut.edu.cn

Introduction

Bulk metallic glasses (BMGs) possess the potential to become a variety of structural materials due to their outstanding mechanical, chemical, and physical properties (Johnson, 1999; Wang et al., 2004). Unfortunately, they usually exhibit a brittle-fracture behavior under freestanding loadings at room temperature, such as upon the uniaxial tension (Schuh et al., 2007). Significant efforts have been made to overcome this shortcoming in recent years with the development of metallic glass matrix composites (MGMCs), consisting of ductile crystals precipitated *in-situ* in a glass-forming matrix (Qiao et al., 2016). The existence of crystals within the amorphous matrix keeps MGMCs from rapidly propagating shear bands, and induces the generation of multiple shear bands. The blocked and mutually interacted shear bands jointly accommodate plasticity, which ensures the distinguishing ductility of MGMCs.

Previous studies have introduced varied MGMCs with excellent tensile ductility (Liu et al., 2018; Liu et al., 2012; Wu et al., 2010). Unfortunately, most of these composites exhibit macroscopic-strain softening with an early onset of necking ascribed to a lack of the work-hardening capacity, which restricts the structural applications for such kinds of *in-situ* MGMCs (Liu et al., 2019). Because of this challenge, the transformation-induced plasticity (TRIP) and twining-induced plasticity (TWIP) mechanisms have been employed in MGMCs through controlling the compositions, and concomitant work hardening, realized in MGMCs. For examples, B2-type MGMCs containing the spherical polymorphousB2 CuZr/Ti precipitates (Wu et al., 2010) and β-type primary β-Zr/Ti solid-solution dendrites embedded in a glassy matrix (Oh et al., 2011; Zhang et al., 2017a; Zhang et al., 2019) are two common *in-situ* MGMCs. The metastable B2 CuZr phase undergoes the martensitic phase transformation during plastic straining, which produces the excellent room-temperature plasticity and work-hardening capacity through TRIP effect (Wu et al., 2010). Furthermore, β-type MGMCs are usually developed by adding β-phase stabilizing elements, such as Nb (Szuess et al., 2001), V(Liu et al., 2019), or Ta (Fan et al., 2017) to promote the primary precipitation of the β solid solution from the glass-forming melts, and work hardening can be observed in such composites.

In addition to the work-hardening mechanisms of MGMCs under tension referred before, the novel *in-situ* Ti-based MGMCs, presented in this study, shows the distinct tensile ductility with the significant work-hardening capability, which is ascribed to the formation of boundaries (Please define boundaries) on the nanoscale. With the help of the finite element modeling (FEM), digital-image correlation (DIC), nanoindentation tests, as well as high-resolution transmission electron microscopy (HRTEM), it is well proved that the ductile dendrites with the remarkable work-hardening capacity act as a prerequisite for achieving the uniform elongation of the MGMCs. The deformation mechanisms are explored by accounting for the competition between the matrix and dendrites upon tensile loading. The generation of DDWs and the development of boundaries on the nanoscale in dendrites during tension induce the marked work-hardening behavior. On the other side, the nucleation and propagation of shear bands within the matrix lead to softening. Moreover, a model has been developed to study the deformation behavior of the composites, the work-hardening coefficients, "n". The "n'" obtained through the model indicates the hardening originated from boundaries on the nanoscale in dendrites and softening induced by shear banding within the glass matrix. The experimental results together with the developed constitutive relations can clearly unveil the work-hardening mechanisms of such kinds of composites. What's more, the current findings extend the fundamental understanding of the deformation mechanisms of MGMCs upon tension, and pave a way to design MGMCs with the significant uniform elongation at room temperature to avoid the early failure.

Experimental

The *in-situ* $Ti_{41}Zr_{32}Ni_6Ta_7Be_{14}$ [atomic percent (at.%)] MGMCs were prepared by arc melting the mixture of pure elements [purity > 99.9 weight percent (wt.%)], Ti, Zr, Ni, Ta, and Be, under a Ti-gettered argon atmosphere. The ingots were re-melted at least four times in a high-purity argon atmosphere to ensure the chemical homogeneity. Copper-mold casting was used to fabricate plate-shape samples, and the size of the samples is 2 mm in thickness and 10 mm in width. The structures of phases in the as-cast ingots were characterized by the X-ray diffraction (XRD; Ultimalv) with the Cu-K_α radiation. Microstructures and chemical compositions were analyzed by the scanning electronic microscopy (SEM; TESCAN, LYRA 3 XMH) combined with the energy-dispersive spectrometry (EDS). The tensile samples, which has been cut into a dog-bone-like shape [10 mm (length) × 2 mm (width) × 2 mm (thickness)]. The tensile experiments at room temperature were conducted with an Instron 5969 testing machine at a strain rate of 5×10^{-4} s^{-1}. To confirm the reproducibility of the tests, at least three specimens were conducted. The evolution of local strains during the experiments was detected by the digital image correlation (DIC) using the MatchID system (Please give references). For these tests, white paint was sprayed on one side of the samples and then coated with black spots in order to increase the contrast of the images taken during the DIC experiments. The XRD, SEM, transmission electron microscopy (TEM), and HRTEM in a JEM-2010 microscope were selected to check the failed samples. Mechanical grinding was the first step when preparing the TEM specimens, and then was ion milling (ion energy: 4.5-5 keV). The hardness and Young's modulus required in the present work were calculated by the results of nanoindentation.

Deformation models have been developed in the current work, which focused on the formation and evolution of deformation bands in the present composite. The deformation behavior of the monolithic BMGs is generally described by the free-volume model and the mechanism-based strain-gradient plasticity model (Rao et al., 2019). A finite element code (ABAQUS) works as user material subroutines in the model. It is noted that the shear bands in the glass matrix and slip bands in dendrites, which are induced by the concentration of free volumes and pill-ups of dislocation, respectively, were an internal state variable, SDV1, in the code. In the current work, a two-dimension (2-D) plane-strain finite element model (FEM) was chosen. As a similar model in the previous work by Rao et al. (Rao et al., 2019), the loading boundary in this model is perpendicular to the loading direction. The normal constraints appear opposite to the loading boundary, and the full constraints appear at a vertex of the opposite boundary. The materials parameters of the glassy and dendrites phases used in the simulation were listed in Table 1. Three varied parameters for dendrites have been made in the FEM, named by dendrites 1, 2, and 3, respectively. The simulative result obtained using dendrites 2 presented the similar deformation behavior with the current MGMCs. The corresponding parameter settings had been discussed previously (Rao et al., 2019).

Table 1 Material parameters used for the FEM modeling of the current MGMCs

Materials parameters for the glassy phase
$E_M = 109.3\ GPa,\ \ v_M = 0.33,\ \ \alpha = 0.8,\ \ \xi_0 = 0.0465,\ \ \chi = 1.25,\ \ v^* = 20\ \mathring{A}$
$T = 300\ \text{K},\ \ \ t_0^{-1} = v_0 \exp\left(-\Delta G / k_B T\right) = 324\ \text{s}^{-1},\ \ \ \ \ \tau_0 = 2k_B T / \Omega = 414\ \text{MPa}$

Elastic modulus, E_M , Poisson ratio, v_M , Geometrical factor, α , Initial free volume concentration, ξ_0 , Geometrical parameter, χ , Critical volume, v^* , Absolute temperature, T , Characteristic time, $v_0 \exp\left(-\Delta G/k_B T\right)$, and Reference stress, $\tau_0 = 2k_B T/\Omega$.

Materials parameters for the dendrites 1 (In the following parameters, please put a space between the number and unit.)
$E_P = 67\text{GPa}$, $v_p = 0.36$, $M = 1.0$, $b = 0.256\text{nm}$, $\alpha = 0.33$, $d_p = 2.5\text{um}$ $d_p = 2.5\text{um}$, $\psi = 0.2$, $\dot{\varepsilon}_0 = 1\text{s}^{-1}$, $k_{20} = 18.5$, $n = 12.5$, $N_B = 45$, $\xi = 35\text{nm}$ $m_0 = 10$, $\sigma_y = 900\text{MPa}$

Materials parameters for the dendrites 2 (In the following parameters, please put a space between the number and unit.)
$E_P = 67\text{GPa}$, $v_p = 0.36$, $M = 2.4$, $b = 0.256\text{nm}$, $\alpha = 0.33$, $d_p = 2.5\text{um}$ $d_p = 2.5\text{um}$, $\psi = 0.2$, $\dot{\varepsilon}_0 = 1\text{s}^{-1}$, $k_{20} = 18.5$, $n = 12.5$, $N_B = 45$, $\xi = 35\text{nm}$ $m_0 = 10$, $\sigma_y = 900\text{MPa}$

Materials parameters for the dendrites 3 (In the following parameters, please put a space between the number and unit.)
$E_P = 67\text{GPa}$, $v_p = 0.36$, $M = 1.0$, $b = 0.256\text{nm}$, $\alpha = 0.33$, $d_p = 2.5\text{um}$ $d_p = 2.5\text{um}$, $\psi = 0.2$, $\dot{\varepsilon}_0 = 1\text{s}^{-1}$, $k_{20} = 18.5$, $n = 12.5$, $N_B = 45$, $\xi = 35\text{nm}$ $m_0 = 10$, $\sigma_y = 1200\text{MPa}$

Elastic modulus E_P, Poisson ratio v_P, Taylor factor M , Burgers vector b , Empirical constant α , Effective Particle size d_P Proportional factor ψ , Reference strain rate $\dot{\varepsilon}_0$, Dynamic recovery constant k_{20} , Power exponent relating to the dislocations annihilation n , Maximum number of dislocation loops N_B , Viscosity coefficient m_0 .

Results

Figure 1 is the result from the SEM observations about the as-cast $Ti_{41}Zr_{32}Ni_6Ta_7Be_{14}$ composites. *In-situ* dendrites are continuously distributed within the glassy matrix, as denoted by the arrows. The volume fraction and size of the dendrites were evaluated by the Image pro software (Please give references) from the SEM images, and their values are 49 ± 3 vol.% and 1-2 μm, respectively. In order to clarify the chemical compositions of both phases, the content of the elements Ti, Zr, Ni, and Ta was acquired via the

EDS analysis. Be is hard to detect precisely, since it is very light and completely dissolved in the amorphous matrix (Hays, 1999). Table 2 presents the chemical compositions of both phases. The values given for the composition in the first line correspond to the nominal composition. The glass matrix is enriched in Zr and Ni, and the dendrites in Ti and Ta, similar to other developed *in-situ* Ti-based MGMCs (Oh et al., 2011).

Table 2 The contents of different elements in the present Ti-based MGMCs.

Zone	Ti (at.%)	Zr (at.%)	Ni (at.%)	Ta (at.%)	Be (at.%)
Composite	41	32	6	7	14
Matrix	34.8 ± 0.2	47.2 ± 2.1	12.4 ± 1.8	5.6 ± 0.2	-
Dendrites	47.2 ± 0.5	34.8 ± 2.0	4.0 ± 1.7	14.0 ± 0.4	-

The TEM images of an as-cast sample are shown in Figure 2 to reveal the details of the microstructures. As can be found from Figure 2(a), bright elliptical particles and gray regions correspond to the dendrites and matrix, respectively. The selected-area electron diffraction (SAED) patterns displayed in Figures 2(b) and (c) correspond to the yellow and green regions in Figure 2(a), respectively, and convincingly demonstrate the formation of the body-centered-cubic (bcc) β-Ti dendrites and the amorphous matrix. Besides the diffraction spots from the β-Ti solid solution, additional weak diffraction spots indicated by red circles, corresponding to the red circles in Figure 2(a), at $1/3 \{112\}_\beta$ and $2/3 \{112\}_\beta$ are visible (Zhang et al., 2017b). These spots can be identified as ω-Ti, which is formed by a displacive-shuffle-dominated mechanism during rapid cooling (Banerjee and Williams, 2013). The deformation mechanisms are closely related to the intrinsic compositions of the composites. In particular, special attention has been directed towards the Ti-based alloys developed by adding the β-phase or α-phase stabilizing elements (Banerjee and Williams, 2013). In view of MGMCs, thermo-mechanical processing of Ti-based alloys (the dendrites) involves deformation in the different phases depending on the compositions, and the change of the β-phase stabilizer (Ta) in the dendrites affects the phase stability, which influences the structure and deformation mechanisms of MGMCs upon loading (Banerjee and Williams, 2013; Marteleur et al., 2012).

The XRD patterns of as-cast and deformed samples are shown in Figure 3. Sharp peaks, denoted crystalline phases, can be found to be superimposed on a broad diffuse diffraction background, denoted amorphous phases, which indicates the existence of bcc β-Ti and amorphous phases, respectively. The XRD patterns after tensile deformation exhibit the same set of diffraction peaks and no additional peaks, confirming that there is no phase transformation upon plastic deformation.

Figure 4(a) displays a characteristic tensile true stress-true strain curve of the composite at ambient temperature. Apparently, the MGMC exhibits a distinct work-hardening behavior. It yields at 1,200 ± 45 MPa, followed by increasing the flow stress, and finally reaches an ultimate tensile strength (UTS) of 1,640 ± 37 MPa and a total uniform strain of 5 %. The plastic deformation is susceptible to the localized deformation (necking), and the Considére criterion can be used to detect necking (Dieter, 1961).

$$\frac{d\sigma}{d\varepsilon} \leq \sigma$$

(1)

where σ is the true stress, and ε is the true strain. The work-hardening rate ($d\sigma/d\varepsilon$) calculated from the true stress-true strain curve inset in Figure 4(a). Comparing these two curves in Figure 4(a) reveals that necking does not happen until the final fracture, and the value of the work-hardening rate exceeds the tensile stress during the whole plastic-deformation stage. In other words, the significant work hardening without macroscopic necking dominates when the composite is subjected to tensile straining.

Different slopes shown in C-J plot ($d\sigma/d\varepsilon$ vs. ε) provide insight into possible changes in deformation mechanisms. Multi-stage work-hardening behavior, which is common in crystalline alloys with remarkable work-hardening, is evident in the present composite [Figure 4(a)] (Li et al., 2018; Yang et al., 2017). The fracture morphology of the samples after tension is displayed in Figure 4(b). Profuse shear bands indicate the large plastic deformation for the present MGMCs. The inset in Figure 4(b) presents an image of a fractured sample. Apparently, the tensile failure of the current composite occurs in a shear fracture mode. Three fracture angles (57.7 °, 77.6 °, and 90 °) exist on the fracture surface. Zhang et al. have reported that the tensile fracture angle is 54 ° in monolithic Zr-based BMGs (Zhang et al., 2003). The tensile fracture angles are larger in the present MGMC, indicating that both normal and shear stresses act on the fracture plane.

The detailed deformation structures in the fractured samples after tension are presented in Figure 5. Figures 5(a) and (b) show the TEM images of a fractured specimen. Compared with the as-cast sample shown in Figure 2(a), DDWs are frequently found within the dendrites along the interface within the glass matrix. Figure 5(c) presents a HRTEM image of the boundary, represented by red lines in the figure. It indicates that the boundary on a nanoscale forms at the interface between the matrix and dendrites during tensile deformation. The fast Fourier transform (FFT) patterns inserted at the left-hand bottom side of Figure 5(c) correspond to the areas of the glass matrix and dendrites, denoted by the squares, A and B, respectively. Figure 5(d) displays a HRTEM image of the glass matrix taken from an area, where a shear band (the light region bordered by red lines) was coincidently caught. The shear band is blocked by a crystal (c.f., the ordered lattice within the yellow ellipse).

In crystalline alloys, slips and dislocations are the major carriers of plasticity. In contrast, the plastic deformation in a glassy phase is accommodated by shear bands. Shao et al. have reported that two-zone shear bands (one is a solid-like zone, and the other a liquid-like zone) control the plasticity of metallic glasses (Shao et al., 2013). This trend can be inferred from the structure in Figure 5(d). The generation of a liquid-like zone (the area between the red lines), surrounded by a solid-like zone, is prevented by the crystalline dendrites (the area within the yellow ellipse), which retards the plastic instability. The crystals in MGMCs can hinder or distribute the expansion of shear bands within the matrix. Figures 5(e) and 5(f) display the magnified HRTEM images of the dendrites. The region close to the interface is indicated in Figure 5(e), corresponding to the area between red lines in Figure 5(c). The dislocations, denoted by "T", severe lattice distortion, represented by yellow circles, and diverse lattice orientations are simultaneously present. The SAED pattern in Figure 5(e) demonstrates the formation of sub-grains and nanocrystals near boundaries. Figure 5(f) depicts the area far away from the boundary. Lattice distortions and dislocations can be observed, corresponding to the inverse FFT image, shown at the left bottom of the figure. The inset in the upper right corner exhibits the corresponding SAED pattern, which demonstrates that the interior of the dendrites retains the bcc structure of β-Ti, and no phase transformation happens. As a result, boundaries on the nanoscale are generated at the interface. The boundaries possess disparate crystalline structures, i.e., neither the structure of the glass matrix nor bcc β-Ti of dendrites.

Figure 6 illustrates the strain-increment-distribution curve upon tensile loading, as obtained by DIC. Figure 6(a) show the strain-distribution maps. The location of fracture, marked by the blue rectangle in Figure 6(a), corresponds to the fracture, the inset shown in Figure 6(b), was selected for the analysis of the temporal strain. The instantaneous strain distribution along the loading direction, extracted from the strain-distribution map near the location of fracture, is presented in Figure 6(b). Obvious necking cannot be found along the gauge length, and the strain increases uniformly during tension except for two inflection points on the instantaneous strain curve at the local strains of 0.7% and 2.7%. The above results signify that shear bands generated locally within the glass matrix are arrested by the ductile dendrites, resulting in the macroscopically-homogenous ductility for the current MGMC.

In order to better understand the deformation behavior, the approach of the finite element model (FEM) was adopted. The uniaxial tensile stress-strain curves of the *in-situ* MGMC are predicted and compared with experiments in Figure 7. The comparison shows a good agreement, indicating that the adopted finite element model is suitable to numerically depict the tensile-deformation behavior of the current MGMC reasonably well. Figures 8(a), (b), and (c) illustrate the evolution of free volumes in the glassy matrix, the dislocation density in the dendrites, and the local stress distribution at a strain of 3%. The corresponding contents for the late deformation stage, 7%, are shown in Figures 8(d), (e), and (f), respectively. It is suggested that homogeneous deformation can be found in the present MGMC at the first time when yielding occurs, as displayed by Figures 8(a), (b), and (c). In contrast, the free volumes and dislocation densities rapidly increase at the strain of 7%, which reveals work softening and hardening in the matrix and dendrites, respectively. What can be observed from Figures 8(d) and (e) is that the region containing a high concentration of free volumes in the matrix [Figure 8(d)] is adjacent to a region, where the dislocation density is relatively high within the dendrites [Figure 8(e)]. This trend confirms that the stress concentration at the interface has an effect on the generation of slip bands in the dendrites and on the initiation of shear bands in the amorphous matrix. Figure 8(f) depicts a map of the strain distribution with respect to the loading direction. Shear localization is not significant. The plastic deformation of the current MGMC under tension is relatively homogenous, as demonstrated in Figure 8(f). These findings are close to the experimental results.

In addition, another two dendrites were selected to make a comparison with dendrites 2 through the FEM analysis, as shown in Figure 9. Figures 9 (a) and (b) demonstrate the results; (a) displays stress-strain curves of varied dendrites and (b) presents stress-strain curves of MGMCs with the corresponding dendrites in (a). It is suggested that dendrite 2 exhibits the excellent work hardening during deformation, and no hardening behavior can be found in the other two dendrites. Consequently, only MGMC 2, with dendrites 2 in-situ the amorphous matrix, demonstrates work hardening during tensile deformation. Figure 10 illustrates the evolution of free volumes within the glassy matrix, the dislocation density in the dendrites, and the local stress distribution at the strain of 5% for three MGMCs. Figures 10(a), (b), and (c) are results of MGMC 1, (d), (e), (f) represent MGMC 2, and (g), (h), and (i) display MGMC 3. The evolution of free volumes is similar among the very three MGMCs [(a), (d), and (g)], which means that the matrix undergoes softening. Obviously, a higher dislocation density forms in MGMC 2 [(b), (e), and (h)]. It is noted that the local stress distribution is more homogenous in MGMCs 2 and 3 when compared to MGMC 1.

Discussion

The results described above indicate that boundaries on the nanoscale observed during tensile loading plays an important role in achieving work hardening of the present composite. Actually,

asynchronized deformation and individual deformed mechanisms occurred between the matrix and dendrites before the formation of boundaries on the nanoscale. In the previous work, it can be found that a disparity of the elastic limits, Young's moduli, and yielding strengths exists between the glass matrix and dendrites in such kinds of composites (Zhai et al., 2017; Zhang et al., 2019). Consequently, the plastic deformation firstly happens within dendrites when the matrix is still at the stage of elastic deformation, and DDWs generated in dendrites begin to develop at the same time. Simultaneously, shear bands are poised for the activation and propagation within the matrix. Multiple shear bands will exist when the matrix undergoes plastic deformation, which is induced by increasing straining. After both phases enter into the plastic deformation, the interaction between shear bands and DDWs assists the development of boundaries on the nanoscale at the interface. It is noted that work hardening and softening control the tensile deformation behavior of the dendrites and matrix, respectively, which results in the intrinsically-soft dendrites transforming into hard ones, and the relative hard glass matrix turning into a soft phase.

Dislocation pile-up

Plastic deformation firstly occurs in the soft dendrites as soon as multiple dislocations operate during tension. The DDWs observed within plastically-deformed dendrites identify a continuous pile-up of dislocations upon successive straining. Only when dislocation pile-ups develop, i.e., dislocation movement is effectively impeded by grain boundaries (Tóth et al., 2010), twins (Fan et al., 2017), or interfaces (phase boundaries) (Guo et al., 2014), successive work-hardening will be available. To better understand the deformation mechanisms, FEM has been employed to study different parameters corresponding to various dislocation densities in the dendrites. Three defect densities (1×10^7, 5×10^{14}, and 1.5×10^{15}/m^2) were chosen for the FEM simulations.

Figure 11 shows the calculated stress-strain curves for the different dislocation densities, and the inset is the corresponding work-hardening rate curve. The results indicate that increasing dislocation densities leads to more pronounced work-hardening. Figure 12 displays maps of the dislocation density (left column), the free-volume density (center), and strain contours (right) for MGMCs with different dislocation densities in the dendrites at a strain of 5%. The top row corresponds to a dislocation density of 1×10^7/m^2 in the dendrites, while the middle row displays the results for a dislocation density of 5×10^{14}/m^2. The bottom images in Figure 12(g-i) represent the findings for a defect density of 1.5×10^{15}/m^2. Consistent with our expectations, successive dislocation multiplication and pile-up contribute to distinct work-hardening in the current composite. Usually, pile-up of dislocations is not achieved and shear banding prevails, accompanied by softening after yielding in other *in-situ* dendrite-reinforced MGMCs (Hays et al., 1999; Liu et al., 2019). In other words, the increase and pile-up of dislocation are important reasons of the work hardening in such type of composites.

Work-hardening behavior during tension

As reported before, three stages can be found in the deformation stage of MGMCs, i.e., elastic-elastic, elastic-plastic, and plastic-plastic stages[34,35]. Coincidentally, the tensile strain-hardening rate of the present MGMC can be accordingly divided into three stages, as displayed in the inset of Figure 4(a) and marked as A, B, and C stages. A similar situation can be often found in a variety of crystalline alloys, including Mg-alloys (Yi et al., 2006), alloys exhibiting the transformation-induced plasticity (TRIP) (Grässel, 2000), twining-induced plasticity (TWIP) steels (De Cooman et al., 2018), and high-entropy

alloys (HEAs)(Ma et al., 2017). The work-hardening rate first decreases, then remains constant (stage A), and subsequently decreases again (stages B and C) with increasing strain.

At Stage A, for the present composites, the dendrites have entered into the plastic range when the glass matrix still keeps in the elastic range. The first decrease of the work-hardening rate occurs at the initial state when the dendrites in the composite yield (i.e., the work-hardening rate enters into the non-linear deformation stage), which is governed by the dislocation glide within the crystalline dendrites. During this stage, the dislocations generated in the dendrites move towards the interface, and pile-up near the interface, as demonstrated in Figures 5(a) and (b). Meanwhile, dislocations within dendrites can diffuse into the matrix and become absorbed by the matrix. The work-hardening rate in Stage A is controlled by the successively-increasing dislocation density, effectively restricting the dislocation slip. It is noted that the start of Stage A at the strain of 0.7% corresponds to the first inflection points shown in Figure 6(b), which indicates the yield point of the dendrites. The other point in Figure 6(b) regards as the stage when the profuse formation of shear banding in the glass matrix, i.e., the beginning of work softening. At the same time, the multiple dislocations generated within dendrites move towards the phase boundary, forming DDWs. The loosely-bonded free-volume regions, which act as flow defects in the glass matrix, can continuously accumulate before the occurrence of plastic deformation. It is noted that softening (i.e., the generation of shear bands) in the glass matrix can be ignored during the elastic-plastic stage.

Hence, the plateau of the work-hardening rate in Stage A corresponds to Stage Ⅱ in traditional crystalline alloys (Dieter, 1961). It provides an extended work-hardening capacity stretching over about 22 % of the whole plastic-deformation stage, in a good agreement with crystalline alloys (Challa et al., 2014). The DDWs and free-volume regions appear synchronous near the phase boundary, which can serve as the foundation of the formation of the heterogeneous structure at the interface.

After Stage A, the propagation of shear bands becomes prevailing at the whole Stage B. It has been speculated that the glass matrix generally exhibits softening due to the localized structural and thermal shearing (Johnson, 1999; Qiao et al., 2016). Accordingly, the work-hardening rate begins to decrease. Nevertheless, the overall deformation behavior remains hardening at this stage. It should be emphasized that the blocking of work-hardened dendrites to the prompt propagation of shear bands is significant, as demonstrated in Figures 4(b) and 5(d).

With even more plastic straining, the dislocation density reaches a dynamic equilibrium state. The dislocation rearrangement becomes active, which is one of the sources for the grain-boundary migration and the generation of nanocrystals (Guo et al., 2014; Zhu et al., 2004). As a result, the interface between the two phases forms a unique boundary structure, which is similar to the results proposed by Huang et al. (Huang et al., 2014). Noted that the boundary on the nanoscale discussed in the current work originates from a hierarchical microstructure, not a chemical composition heterogeneous structure, as investigated in Huang's work (Huang et al., 2014). The HRTEM and SAED images in Figure 5(e) show the existence of nanocrystals, which suggests that the interface between the two phases evolves into boundaries on the nanoscale, and the inner part of the dendrites remains the original structure. The heterogeneous structure induced by the formation of special boundaries is particularly beneficial and has an overarching effect on maintaining work-hardening in Stage B (Roters, 2000). On one hand, plasticity gradients are built up, which contributes to the blockage of the dislocation movement, accompanied by continuous work-hardening in dendrites. On the other hand, as reported by Wang et al.(Wang et al., 2007), the interface between both phases exhibits unique inelastic shear-transfer characteristics, where the glass matrix acts as the high-capacity sink enabling the absorption of plasticity.

As the overall effect, both the successive dislocation pile-up within dendrites and the profuse shear bands in the glass matrix accommodate the plasticity.

Stage C is the final stage, where the work-hardening rate is lower than the true stress [Figure 4(a)]. Plastic instability occurs at this stage. On the basis of the results in Stage B, the glass matrix undergoes pronounced softening upon plastic deformation, which is attributed to the shear-induced local dilatation (Bei et al., 2006). In contrast, the dendrites are strongly hardened. The boundaries on the nanoscale segregate the matrix and dendrites, and the trilaminar heterogeneous structure forms. While the dislocation generated in dendrites has saturated, which means that defects, such as cracks, have formed in dendrites at this stage. Hence, multiple mature shear bands appear in the matrix, and the dendrites cannot stop them. At this stage, the work-softening mechanisms generated in the glass matrix become more pronounced, while the work-hardening mechanisms generated in dendrites weaken.

The hardness of the matrix and dendrites before and after tension have been measured by nanoindentation tests. The Berkovich diamond indenter tip penetrates into the matrix and dendrites, respectively, when conducting nanoindentation tests, and the maximum indentation depth sets as 1,000 μm. At least ten points were selected during nanoindentation experiments. The results are summarized in Table 3, which verifies the distinctly-different deformation behaviors of the two phases. The initial hard (glass matrix)/soft (dendrites) model of the MGMC changes into a soft (glass matrix)/hard (dendrites) model after tension, which is caused by the particular deformation mechanisms (Please describe these mechanisms) described above. No macroscopic necking is found, since the composite fails immediately when the plastic instability is reached. On the whole, a homogenous plastic elongation is dominant upon tensile loading.

Table 3. The hardness values of the glass matrix and the dendrites before and after tensile testing measured by nanoindentation. Where are the results of the as-cast sample?

Type of specimen	Matrix (GPa)	Dendrites (GPa)
As-cast	6.96 ± 0.21	4.58 ± 0.45
Deformed	6.18 ± 0.13	6.22 ± 0.27

Constitutive relationship

On the basis of the present and previous findings (Fan et al., 2017), some implications can be drawn. A transition of different tensile deformation mechanisms corresponding to the various stages upon deformation occurs in the current composites.

At the beginning, both phases of the current composite are under the elastic state, and attempts to learn ???? the Young's moduli for each phase and composite have been made. Generally, the average Poisson ratio of most BMGs could be assumed as a similar value to crystalline phases (Qiao et al., 2016; Wang, 2012). Hence, for the further considerations the Poisson ratio here is set for 0.33 in both phases (Wang, 2012). One of the attempts can be established according to Hashin and Shtrikman, as follows (Hashin, 1963):

$$E_c = E_m \left[1 + \frac{f_v \left(E_d - E_m \right)}{\left(1 - f_v\right)\beta\left(E_d - E_m\right) + E_m} \right]$$, (2)

where E_c, E_m, and E_d are the Young's moduli of the composite, the matrix, and the dendrites,

respectively, the value of f_v is 0.49, which represents the volume fraction of dendrites, β is constant,

and $\beta = \dfrac{8 - 10v_m}{15\left(1 - v_m\right)}$, and v_m (0.33) is the Poisson ratio of the matrix. E_m and E_d are equal to 109 and

83 GPa, respectively. Therefore, E_c can be calculated as 95.5 GPa by inserting these parameters into Eq. (2). In addition, another one is the simple rule of mixtures (ROM), as follows:

$$E_c = E_m\left(1 - f_v\right) + E_d f_v$$. (3)

The value of E_c is 96.3 GPa, similar to the results obtained by Eq. (2).

With increasing strain, the soft dendrites yield first. On the basis of the ROM, the stress of the composite can be established as:

$$\sigma_c = f_v \sigma_d + \left(1 - f_v\right)\sigma_m$$, (4)

where σ_c, σ_d, and σ_m are the tensile stresses of the composite, dendrites, and glass matrix, respectively. An overall strain (ε) of 1.5 %, a median of this stage, is chosen as an input into Eq. (4), which equates to: $\left(1 - f_v\right)E_m \varepsilon = \left(1 - 0.49\right) \times 109 \times 0.015 = 833$ (MPa). Referring to Figure 4(a), the

stress at the strain of 1.5% is about 1,200 MPa. As a result, σ_d can be calculated as 749 MPa.

The constitutive equation of the composites at this stage can be expressed according to (Xia and Wang, 2010):

$$\sigma = \frac{1}{\sqrt{3}c_d}\left[\sqrt{3}\sigma_d + 3E_m\left(1 - \beta\right)\frac{1 - f_v}{f_v}\frac{\varepsilon^p}{\sqrt{3}} \right]$$, (5)

where c_d and c_m are the average stress-concentration factors of the dendrites and the matrix,

respectively ($c_m = \dfrac{\beta\left(E_d - E_m\right) + E_m}{\left[f_v + \left(1 - f_v\right)\beta\right]\left(E_d - E_m\right) + E_m}$, $c_d = \dfrac{E_d}{\left[f_v + \left(1 - f_v\right)\beta\right]\left(E_d - E_m\right) + E_m}$). ε^p is the

plastic strain of the composites, which is given as $\varepsilon^p = f_v c_d \varepsilon_d^p$, and ε_d^p is the plastic strain for

dendrites. Consequently, Eq. (5) can be written as: $\sigma = \sigma_d + 0.28 E_m \varepsilon_d^p$. As presented in Figure 6(b), the yield strain of the dendrites is about 0.7%, and this yield strain of the dendrites in the

current MGMC is highly consistent with other Ti-based MGMCs (Fan et al., 2017; Qiao et al., 2016).

Consequently, the plastic strain of the dendrites, ε_d^p, at the overall strain of 1.5 % is about 0.8 %. According to Eq. (5), the stress acting on dendrites at the overall strain of 1.5 % is calculated as 950 MPa, very close to the stress in dendrites of other Ti-based MGMCs and Ti-based crystalline alloys (Dieter, 1961; Qiao et al., 2016). The model in Eq. (5) is more suitable for interpreting the stress conditions at this stage. The yield stress for dendrites is about 580 MPa, according to Hooke's law. The work-hardening exponent, n, is estimated to be 0.66.

Both phases undergo plastic deformation at this stage when the glass phase begins to yield. This stage corresponds to the decrease of the work-hardening rate, as shown in Figure (4b). For a dislocation-free crystal, it has been postulated by Frenkel (Frenkel, 1926) that the theoretical shear strength can be assumed to be $\tau_y \cong G/5$. Therefore, the yield strength of the glass matrix can be calculated as 1,640 MPa ($\sigma_{ym} = 2\tau_y$) (Johnson and Samwer, 2005). The tensile stress of the current composite in this stage is given by (Xia and Wang, 2010):

$$\sigma = \frac{1}{\sqrt{3}c_m}\left[\sqrt{3}\sigma_{ym} - 3E_m(1-\beta)\frac{\varepsilon^p}{\sqrt{3}}\right] , \qquad (6)$$

and Eq. (6) can be simplified as: $\sigma = \sigma_{ym} - 0.524E_m\varepsilon^p$. In another way, the tensile stress-strain relation of the matrix in the P-P stage can be represented as (Xia and Wang, 2010):

$$\sigma = \sigma_{ref}(\sigma_{ym}/E_m + \varepsilon^p)^{n'} , \qquad (7)$$

where σ_{ref} is the reference stress of the matrix during uniaxial tension, and $\sigma_{ref} = \frac{E_m^{n'}}{\sigma_{ym}^{n'-1}}$, n' is the work-hardening coefficient of the matrix. The work-softening strain of the P-P stage can be inferred at a strain of 3.0 % [Figure 4(a)], which is close to the second inflection point displayed in Figure 6(b). Combining Eqs. (6) and (7), the work-hardening coefficient of the matrix at this stage can be calculated as - 0.069. This trend indicates that the work hardening in the dendrites is more pronounced than softening induced in the glass matrix, which results in the excellent work hardening in the current composite. Such a situation is in line with the experimental data (c.f., Table 3). Table 3 reveals that the hardness of the matrix decreases while that of the dendrites increases upon tensile deformation. The dendrite hardness becomes higher than that of the glass matrix, suggesting that the work-hardening effect overcomes the softening effect. A comparison of the hardness values of the dendrites and matrix for a variety of different MGMCs is summarized in Figure 13 (the literature data were taken from Refs. (Joseph et al., 2017; Kolodziejska et al., 2016; Lee et al., 2004; Zhang et al., 2016). The hardness of the dendrites will be higher than that of the matrix after tension for composites with a significant work-hardening capacity. In other words, dendrites with a higher hardness than the matrix are beneficial for work hardening in composites. Furthermore, the FEM results obtained above also confirm the conclusions. The deformation behavior of dendrites 1 to 3 can be regarded as different deformation stages of MGMC 2 during tension. Dendrite 1 presents the initial state, and dendrite 3 is the final state induced by work hardening (dendrite 2). The MGMC 1 with a soft dendrite 1 displays work softening, and a shear-localization distribution occurred during deformation [Figure 10(c)]. On the other hand, the

MGMC 3 with the hard dendrite 3 shows similar local stress distributions [Figures 10(f) and (i)], which indicates that the hard dendrite phase within the matrix makes MGMCs hardening. The MGMC 2 in FEM is based on the present composite, showing that dendrites change from soft to hard phases during tension. The corresponding work hardening will be achieved at the same time. Hence, it is reasonable to rationalize that the work-hardening capacity in the present composite is a result of the pronounced hardening of the dendrites.

Conclusions

In the present work, deformation mechanisms of the $Ti_{41}Zr_{32}Ni_6Ta_7Be_{14}$ MGMC have been revealed and characterized by experiments and theoretical calculations. The work-hardening behavior in dendrites ascribes to the formation of boundaries on the nanoscale, which is induced by generating DDWs during tensile deformation. On the other hand, softening in the matrix is induced by the formation of shear bands. Combining these factors, the stress condition of the current composites has been studied step by step according to the three deformation stages (Please detail the three stages), thus revealing homogeneously plastic deformation mechanisms. Obviously, the work-hardening ability of the dendrites overcomes the softening of the glass matrix and leads to a significantly-homogeneous tensile elongation.

References

Banerjee, D., Williams, J.C., 2013. Perspectives on titanium science and technology. Acta Materialia 61, 844-879.

Bei, H., Xie, S., George, E.P., 2006. Softening caused by profuse shear banding in a bulk metallic glass. Physical review letters 96, 105503-4.

C. C. Hays., C.P.K???., W. L. Johnson., 1999. Microstructure controlled shear band pattern formation and enhanced plasticity of bulk metallic glasses containing in situ formed ductile phase dendrite dispersions. Physical review letters 84, 2901-1904.

Challa, V.S.A., Wan, X.L., Somani, M.C., Karjalainen, L.P., Misra, R.D.K., 2014. Significance of interplay between austenite stability and deformation mechanisms in governing three-stage work hardening behavior of phase-reversion induced nanograined/ultrafine-grained (NG/UFG) stainless steels with high strength-high ductility combination. Scripta Materialia 86, 60-63.

De Cooman, B.C., Estrin, Y., Kim, S.K., 2018. Twinning-induced plasticity (TWIP) steels. Acta Materialia 142, 283-362.

Dieter, G.E., 1961. Mechanical metallurgy in: Robert, F.M. (Ed.), Mechanical metallurgy. McGraw-Hill, London, p. 290.

F. Roters, D.R., G. Gottsten., 2000. Work hardening in heterogeneous alloys-A microstructural approach on three intenal state variables Acta Materialia 48, 4181-4189.

Szuess. F., C.P. Kim., W.L. Johnson., 2001. Mechanical properties of Zr56.2Ti13.8Nb5.0-Cu6.9Ni5.6Be12.5 ductile phase reinforced bulk metallic glass composite. Acta Materialia 49, 1507-1513.

Fan, J., Qiao, J.W., Wang, Z.H., Rao, W., Kang, G.Z., 2017. Twinning-induced plasticity (TWIP) and work hardening in Ti-based metallic glass matrix composites. Scientific reports 7, 1877-12.

Frenkel, J., 1926. Zur Theorie der Elastizitätsgrenze und der Festigkeit kristallinischer Körper. 572-609

Guo, W., Jägle, E., Yao, J., Maier, V., Korte-Kerzel, S., Schneider, J.M., Raabe, D., 2014. Intrinsic and extrinsic size effects in the deformation of amorphous CuZr/nanocrystalline Cu nanolaminates. Acta Materialia 80, 94-106.

Hashin, Z., 1963. A variational approach to the theory of the elastic behaviour of multiphase materials. J. Mech. Phys. Solids, 11, 127-140.

Huang, E.W., Qiao, J., Winiarski, B., Lee, W.J., Scheel, M., Chuang, C.P., Liaw, P.K., Lo, Y.C., Zhang, Y., Di Michiel, M., 2014. Microyielding of core-shell crystal dendrites in a bulk-metallic-glass matrix composite. Scientific Reports 4, 4394-7.

Johnson, W.L., 1999. Bulk glass-forming metallic alloys: Science and technology. MRS Bulletin, 41-56.

Johnson, W.L., Samwer, K., 2005. A universal criterion for plastic yielding of metallic glasses with a (T/Tg) 2/3 temperature dependence. Physical Review Letters 95, 195501.

Joseph, J., Stanford, N., Hodgson, P., Fabijanic, D.M., 2017. Understanding the mechanical behaviour and the large strength/ductility differences between FCC and BCC AlxCoCrFeNi high entropy alloys. Journal of Alloys and Compounds 726, 885-895.

Kolodziejska, J.A., Kozachkov, H., Kranjc, K., Hunter, A., Marquis, E., Johnson, W.L., Flores, K.M., Hofmann, D.C., 2016. Towards an understanding of tensile deformation in Ti-based bulk metallic glass matrix composites with BCC dendrites. Scientific Reports 6, 22563-8.

Lee, J.-C., Kim, Y.-C., Ahn, J.-P., Kim, H.-S., Lee, S.-H., Lee, B.-J., 2004. Deformation-induced nanocrystallization and its influence on work hardening in a bulk amorphous matrix composite. Acta Materialia 52, 1525-1533.

Li, X., Song, R., Zhou, N., Li, J., 2018. An ultrahigh strength and enhanced ductility cold-rolled medium-Mn steel treated by intercritical annealing. Scripta Materialia 154, 30-33.

Liu, Y.Y., Liu, P.Z., Li, J.J., Liaw, P.K., Spieckermann, F., Kiener, D., Qiao, J.W., Eckert, J., 2018. Universally scaling Hall-Petch-like relationship in metallic glass matrix composites. International Journal of Plasticity 105, 225-238.

Liu, Y.Y., Li, J.J., Wang, Z., Shi, X.H., Qiao, J.W., Wu, Y.C., 2019. Prediction of tensile yielding in metallic glass matrix composites. Intermetallics 108, 72-76.

Liu, Z., Li, R., Liu, G., Su, W., Wang, H., Li, Y., Shi, M., Luo, X., Wu, G., Zhang, T., 2012. Microstructural tailoring and improvement of mechanical properties in CuZr-based bulk metallic glass composites. Acta Materialia 60, 3128-3139.

Ma, L., Wang, L., Nie, Z., Wang, F., Xue, Y., Zhou, J., Cao, T., Wang, Y., Ren, Y., 2017. Reversible deformation-induced martensitic transformation in Al 0.6 CoCrFeNi high-entropy alloy investigated by in situ synchrotron-based high-energy X-ray diffraction. Acta Materialia 128, 12-21.

Marteleur, M., Sun, F., Gloriant, T., Vermaut, P., Jacques, P.J., Prima, F., 2012. On the design of new β-metastable titanium alloys with improved work hardening rate thanks to simultaneous TRIP and TWIP effects. Scripta Materialia 66, 749-752.

O.Grässel, L.K., G. Frommeyer, L. W. Meyer, 2000. High strength Fe-Mn-(Al, Si) TRIP/TWIP steels development -properties-application. International Journal of Plasticity 16, 1391-1409.

Oh, Y.S., Kim, C.P., Lee, S., Kim, N.J., 2011. Microstructure and tensile properties of high-strength high-ductility Ti-based amorphous matrix composites containing ductile dendrites. Acta Materialia 59, 7277-7286.

Qiao, J., Jia, H., Liaw, P.K., 2016. Metallic glass matrix composites. Materials Science and Engineering: R: Reports 100, 1-69.

Rao, W., Zhang, J., Kang, G., Yu, C., Jiang, H., 2019. A meso-mechanical constitutive model of bulk metallic glass composites considering the local failure of matrix. International Journal of Plasticity 115, 238-267.

Schuh, C., Hufnagel, T., Ramamurty, U., 2007. Mechanical behavior of amorphous alloys. Acta Materialia 55, 4067-4109.

Shao, Y., Yao, K., Li, M., Liu, X., 2013. Two-zone heterogeneous structure within shear bands of a bulk metallic glass. Applied Physics Letters 103, 171901.

Tóth, L.S., Estrin, Y., Lapovok, R., Gu, C., 2010. A model of grain fragmentation based on lattice curvature. Acta Materialia 58, 1782-1794.

Wang, W.H., 2012. The elastic properties, elastic models and elastic perspectives of metallic glasses. Progress in Materials Science 57, 487-656.

Wang, W.H., Dong, C., Shek, C.H., 2004. Bulk metallic glasses. Materials Science and Engineering: R: Reports 44, 45-89.

Wang, Y., Li, J., Hamza, A.V., Barbee, T.W., Jr., 2007. Ductile crystalline-amorphous nanolaminates. Proceedings of the National Academy of Sciences of the United States of America 104, 11155-11160.

Wu, Y., Xiao, Y., Chen, G., Liu, C.T., Lu, Z., 2010. Bulk metallic glass composites with transformation-mediated work-hardening and ductility. Advanced Materials 22, 2770-2773.

Xia, S.H., Wang, J.T., 2010. A micromechanical model of toughening behavior in the dual-phase composite. International Journal of Plasticity 26, 1442-1460.

Yang, C.L., Zhang, Z.J., Zhang, P., Zhang, Z.F., 2017. The premature necking of twinning-induced plasticity steels. Acta Materialia 136, 1-10.

Yi, S.B., Davies, C.H.J., Brokmeier, H.G., Bolmaro, R.E., Kainer, K.U., Homeyer, J., 2006. Deformation and texture evolution in AZ31 magnesium alloy during uniaxial loading. Acta Materialia 54, 549-562.

Zhai, H., Xu, Y., Zhang, F., Ren, Y., Wang, H., Liu, F., 2017. Effect of transition metal elements (Cu, Ni, Co and Fe) on the mechanical properties of Ti-based bulk metallic glass composites. Journal of Alloys and Compounds 694, 1-9.

Zhang, L., Li, W.Q., Zhu, Z.W., Fu, H.M., Li, H., Li, Z.K., Zhang, H.W., Wang, A.M., Zhang, H.F., 2017a. Distribution of Be in a Ti-based bulk metallic glass composite containing B-Ti. Journal of Materials Science & Technology 33, 708-711.

Zhang, L., Narayan, R.L., Fu, H.M., Ramamurty, U., Li, W.R., Li, Y.D., Zhang, H.F., 2019. Tuning the microstructure and metastability of β-Ti for simultaneous enhancement of strength and ductility of Ti-based bulk metallic glass composites. Acta Materialia 168, 24-36.

Zhang, L., Zhu, Z., Fu, H., Li, H., Zhang, H., 2017b. Improving plasticity and work-hardening capability of β-type bulk metallic glass composites by destabilizing β phases. Materials Science and Engineering: A 689, 404-410.

Zhang, Y., Wu, L., Zhang, J., Xing, J., Luo, J., 2016. Eutectic microstructures and thermoelectric properties of MnTe-rich precipitates hardened PbTe. Acta Materialia 111, 202-209.

Zhang, Z.F., Eckert, J., Schultz, L., 2003. Difference in compressive and tensile fracture mechanisms of Zr59Cu20Al10Ni8Ti3 bulk metallic glass. Acta Materialia 51, 1167-1179.

Zhu, K.Y., Vassel, A., Brisset, F., Lu, K., Lu, J., 2004. Nanostructure formation mechanism of α-

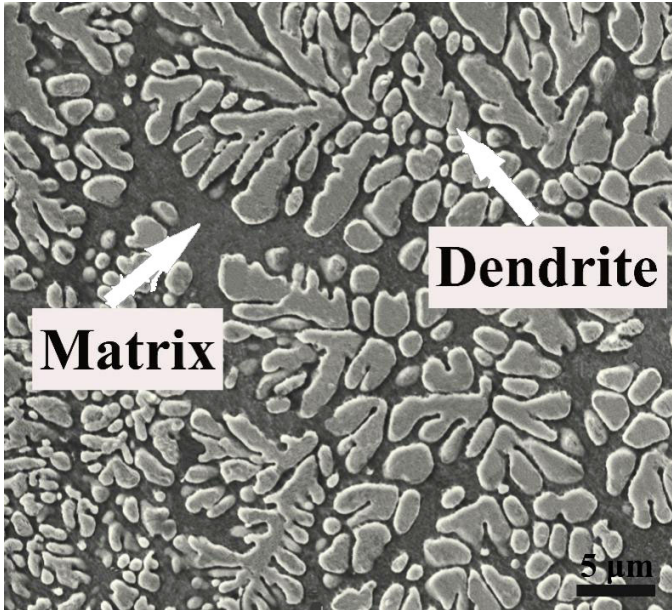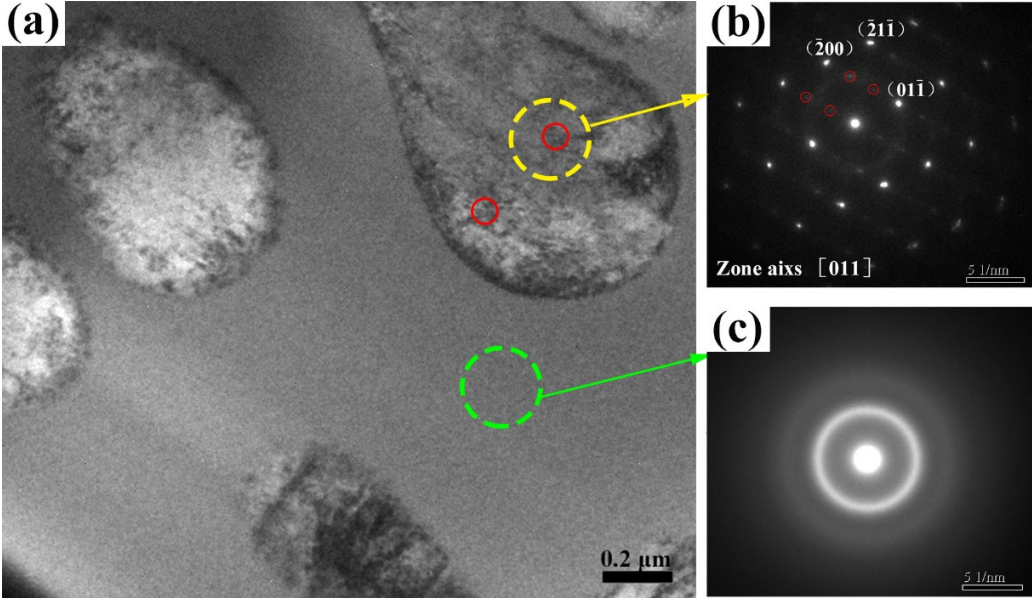titanium using SMAT. Acta Materialia 52, 4101-4110.

Figures

Figure 1.

Figure 2.

Ti$_{41}$Zr$_{32}$Ni$_6$Ta$_7$Be$_{14}$

⬡ —— β-Ti (bcc)

(110)

(200)   (211)   After tension

(220)

As-cast

Intensity (a.u.)

2 theta (deg.)

(a)

Stress (Mpa)

Strain (%)

Strain hardening rate (MPa)
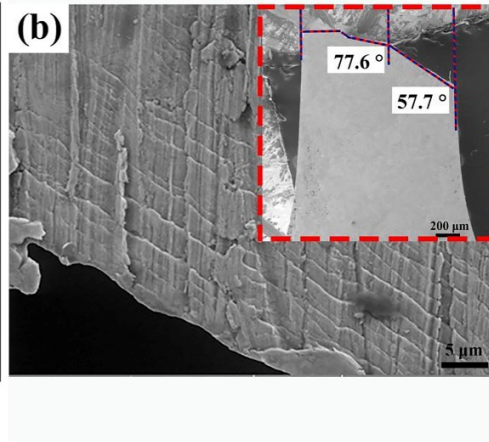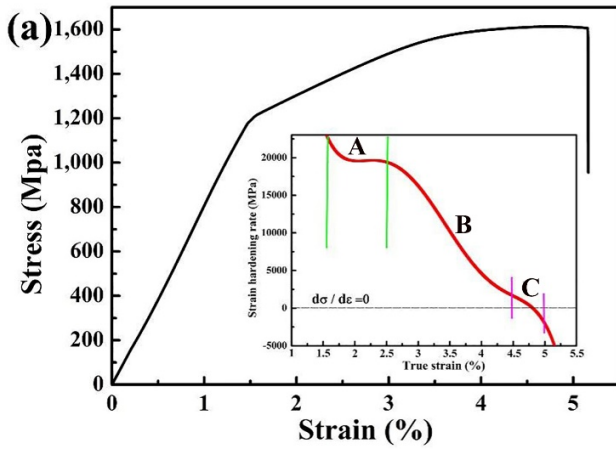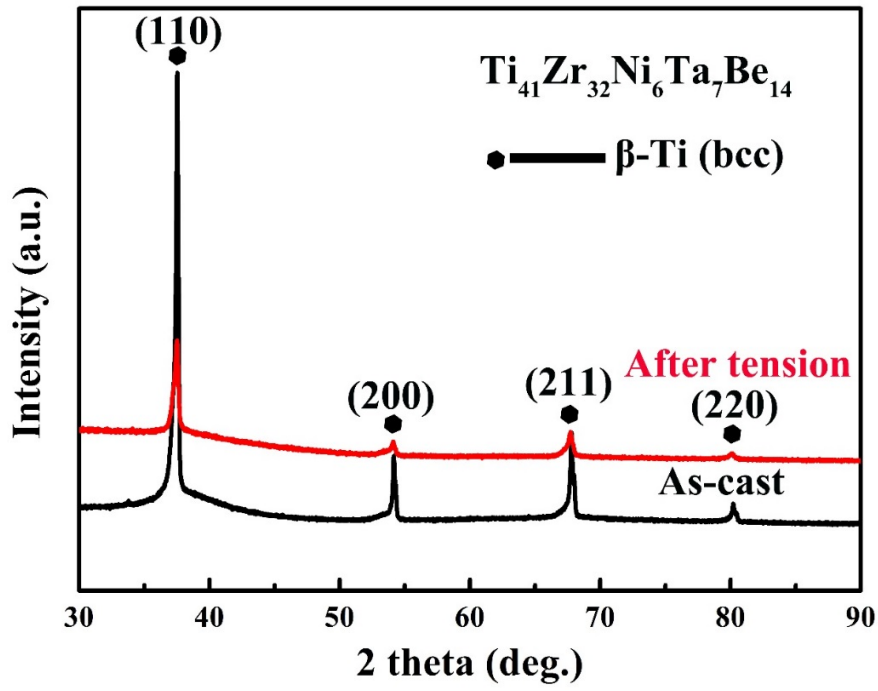
A

B

dσ / dε =0

C
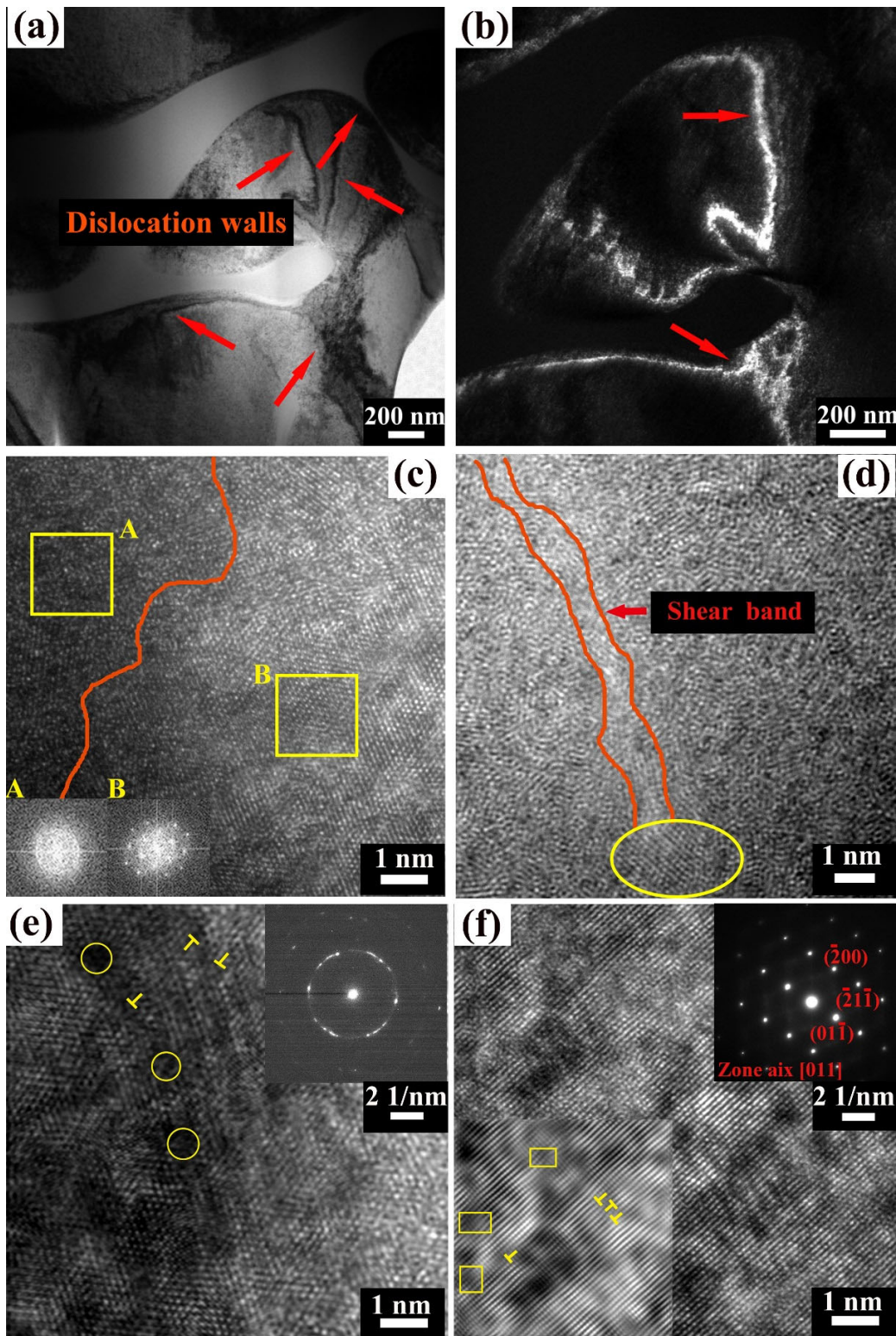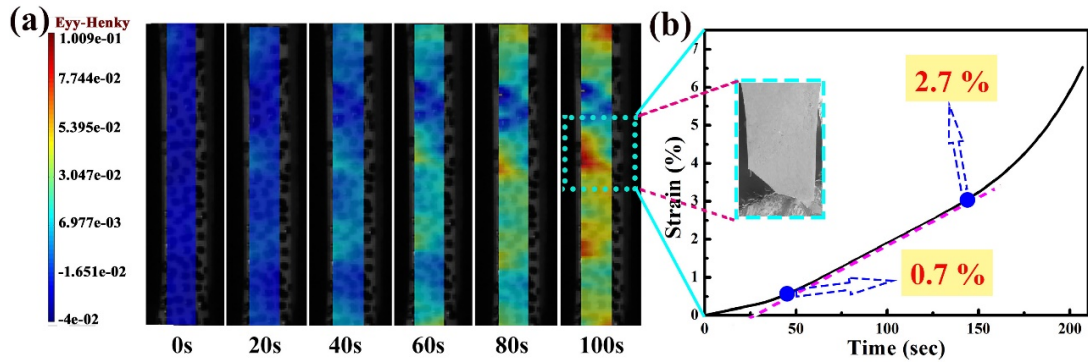
True strain (%)

(b)

77.6 °
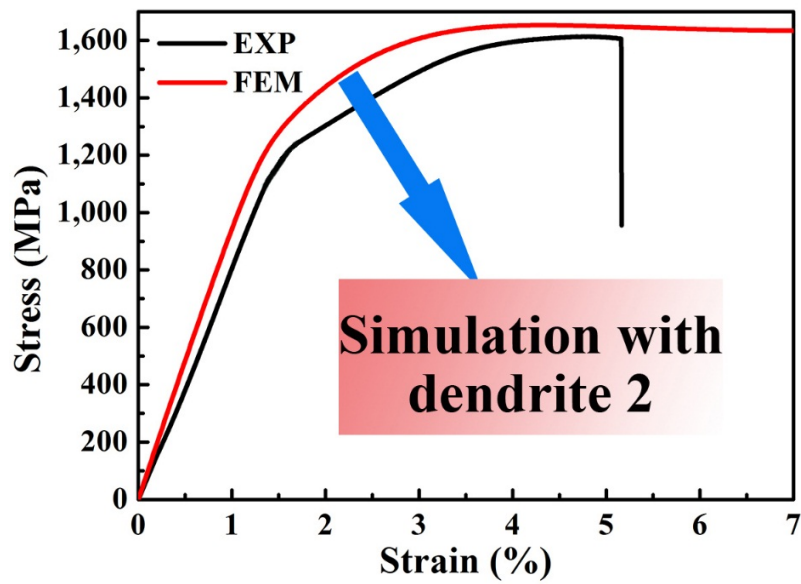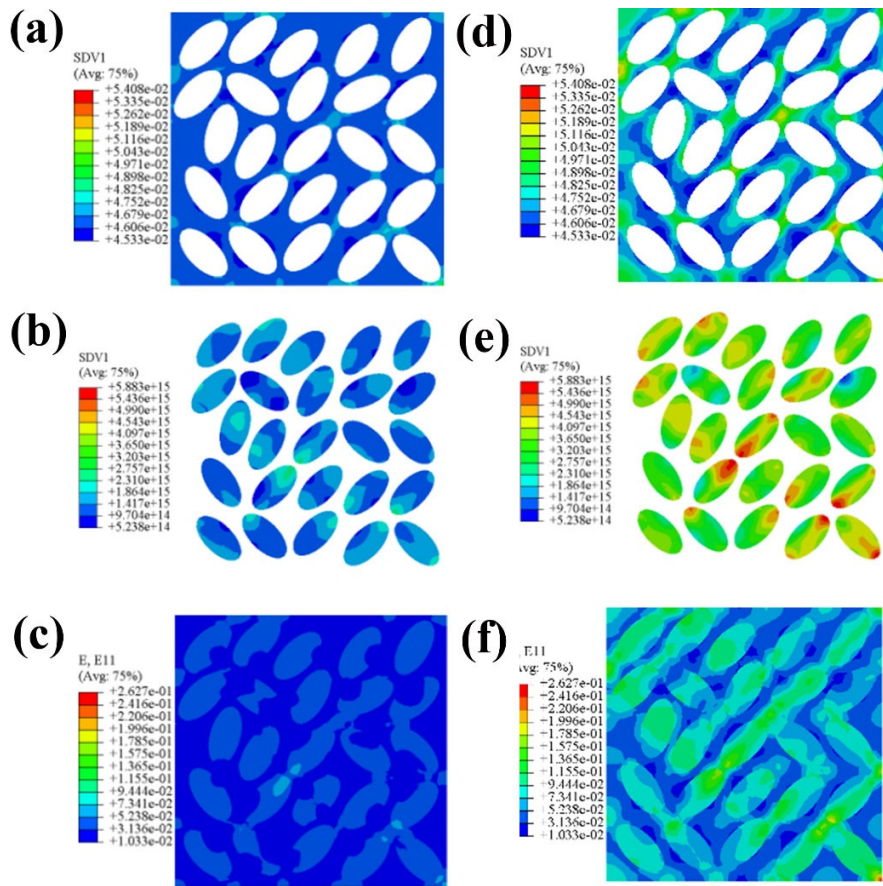
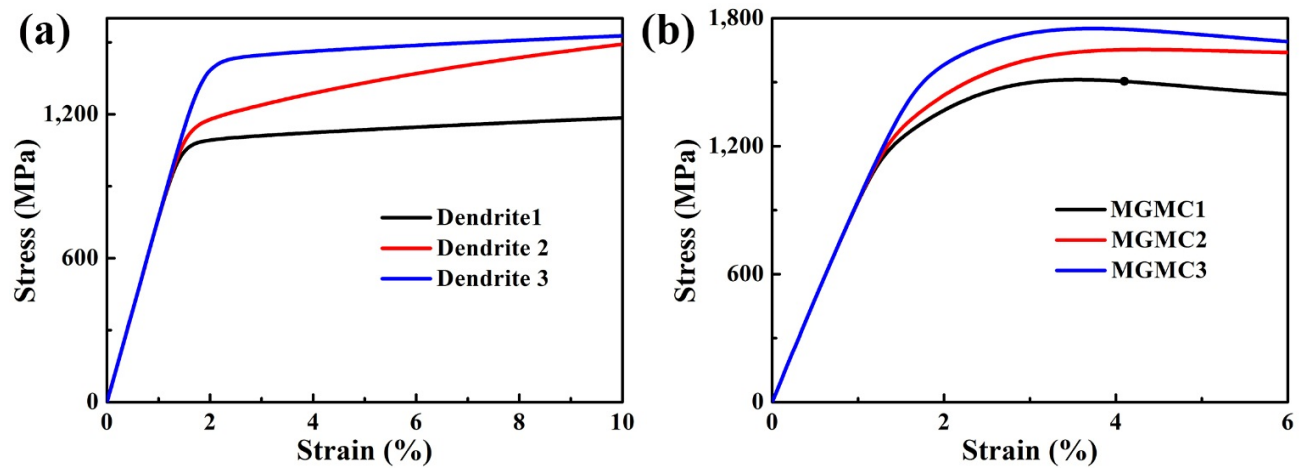57.7 °

200 µm

5 µm

Figure 3.

Figure 4.

Figure 5.

Figure 6.

Figure 7.

Figure 8.

Figure 9.
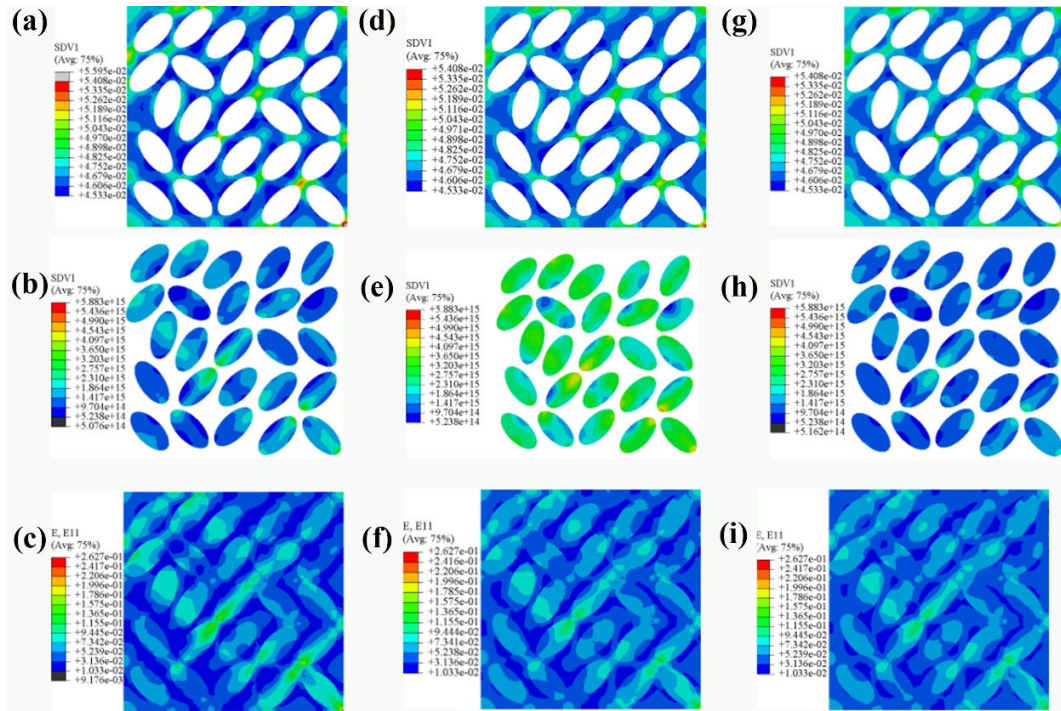
Figure 10.
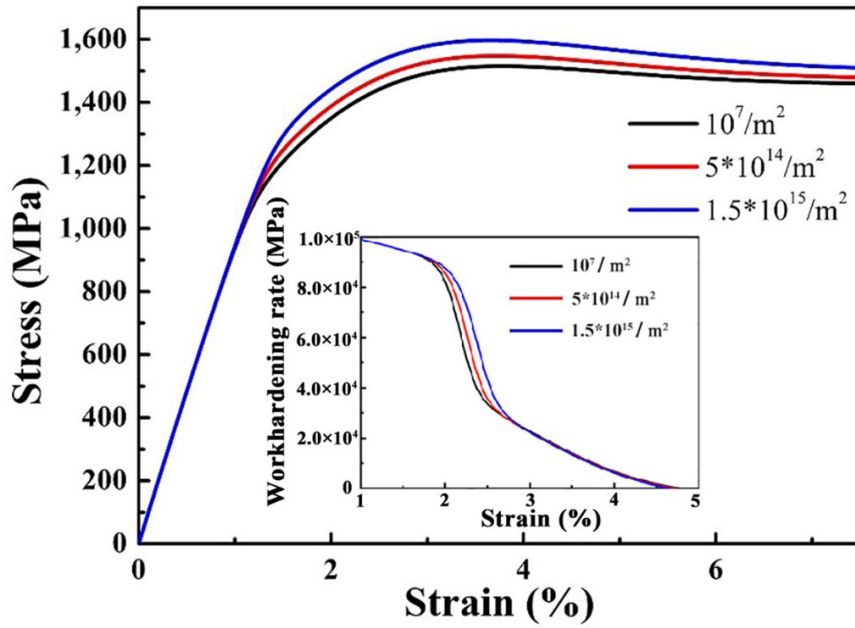
Figure 11.
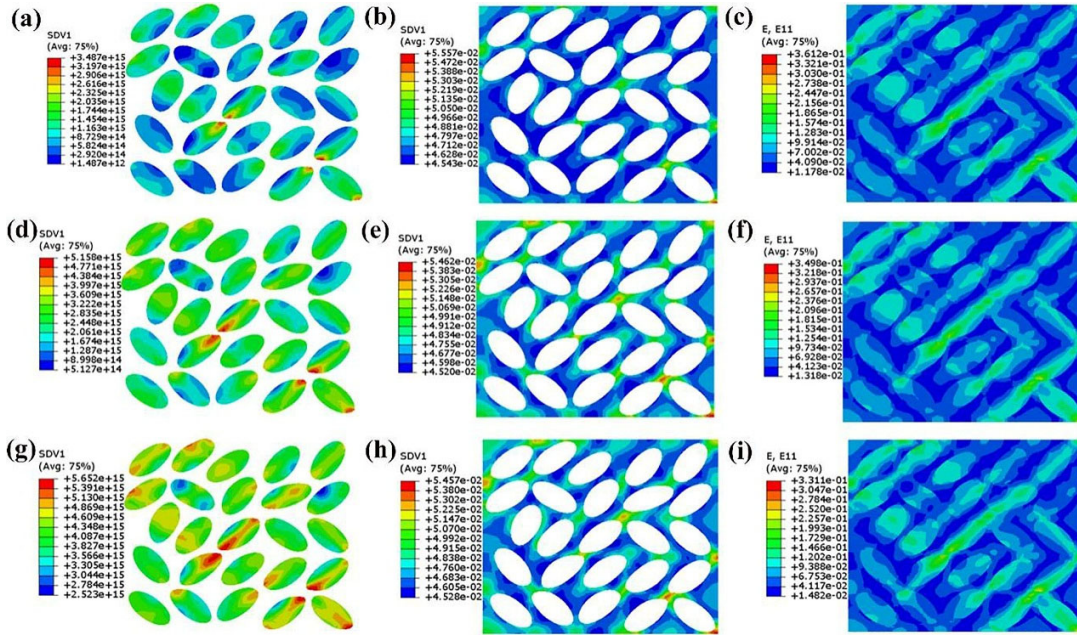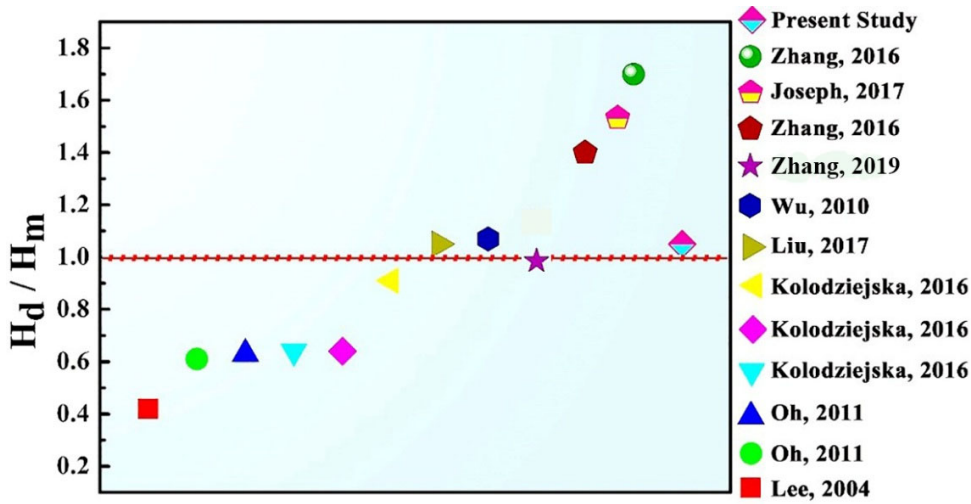
Figure 12.

Figure 13.

Figure Captions

Figure 1. SEM image of the as-cast composite.

Figure 2. Bright-field TEM image of the as-cast composite (a); Selected-area electron diffraction (SAED) patterns corresponding to the crystalline phase and the glass matrix are presented in (b) and (c), respectively.

Figure 3. XRD patterns of the composite before and after tensile deformation.

Figure 4. True stress-true strain curve of the composite (a); the work-hardening rate curve is shown in the inset. (b) are SEM images of a sample after fracture.

Figure 5. TEM images of a sample after fracture. (a) and (b) show bright-field and dark-field TEM images of a fractured sample, respectively. (c) depicts a HRTEM image of the interface between the matrix and dendrites. An image of a shear band in the matrix is presented in (d). (e) and (f) display HRTEM images of the dendrites.

Figure 6. DIC images of the deformed composite. (a) shows the strain distribution with time and (b) gives the corresponding temporal strain curve.

Figure 7. The true stress-true strain curves obtained by the experiment and FEM, respectively.

Figures 8(a), (b), and (c) illustrating the evolution of free volumes within the glassy matrix, the dislocation density in the dendrites, and the local stress distribution at the strain of 3%. And the corresponding contents for the late deformation stage, 7%, shown in Figures 8(d), (e), and (f).

Figure 9. FEM analysis for another two dendrites, (a) stress-strain curves of varied dendrites, and (b) stress-strain curves of MGMCs with the corresponding dendrites in (a).

Figure 10. The evolution of free volumes within the glassy matrix, the dislocation density in the dendrites, and the local stress distribution at the strain of 5% for the very three MGMCs, (a), (b), and (c) are results of MGMC 1, (d), (e), (f) represent MGMC 2, and (g), (h), and (i) display MGMC 3.

Figure 11. Calculated true stress-true strain curves of MGMCs with different dislocation densities in the dendrites, as obtained by FEM, the inset corresponds to work-hardening curves.

Figure 12. Free-volume density and maps of strain contours of the MGMCs with different defect densities in the dendrites at a true strain of 5%.

Figure 13. Ratios of the hardness of the dendrites (Hd) and the matrix (Hm) for different MGMCs.